

Seeing Majorana fermions in time-of-flight images of spinless fermions coupled by s -wave pairing

Jiannis K. Pachos,¹ Emilio Alba,² Ville Lahtinen,³ and Juan J. Garcia-Ripoll²

¹*School of Physics and Astronomy, University of Leeds, Leeds, LS2 9JT, United Kingdom*

²*Instituto de Física Fundamental, IFF-CSIC, Calle Serrano 113b, Madrid 28006, Spain*

³*NORDITA, Roslagstullsbacken 23, 106 91 Stockholm, Sweden*

(Dated: September 25, 2012)

The Chern number, a topological invariant characterising the ground state of fermionic systems, is a definitive theoretical signature that determines whether a given superconducting system can support Majorana zero modes. Here we show that it can be faithfully reproduced through a set of time-of-flight measurements, making it a diagnostic tool also in actual cold atom experiments. We demonstrate the measurement scheme by employing a chiral topological model of spinless fermions that only requires the experimentally accessible s -wave pairing and staggered tunnelling that mimics spin-orbit coupling. By adiabatically connecting this model to Kitaev's honeycomb lattice model, we show that it gives rise to $\nu = \pm 1$ phases, where vortices carry Majorana fermions, and $\nu = \pm 2$ phases that emerge as a collective state of localised Majorana fermions. Hence, the preparation of these phases and the detection of their Chern numbers provides an unambiguous signature for the presence of Majorana modes. Finally, we demonstrate that our detection procedure is resilient against most inaccuracies in experimental control parameters as well as finite temperature.

PACS numbers: 67.85.-d, 03.65.Vf

The discovery of a new particle carries an excitement that reaches well beyond the scientific community. Majorana “fermions” [1], even though they are expected to emerge as zero mode quasiparticles in topological systems, are highly anticipated. This is due to their predicted exotic statistics that is unlike of any other behaviour we have seen so far. Importantly, they offer the possibility of employing their statistics for sophisticated technological applications such as topological quantum computation [2].

For a fermionic system to support localised Majorana zero modes, two conditions need to be satisfied: the spectrum should possess particle-hole symmetry and the ground state should exhibit suitable topologically non-trivial behaviour. Particle-hole symmetry implies that for a stationary state Ψ_E^\dagger with energy E , there exists another state Ψ_{-E} with energy $-E$. The suitable topological character of the ground state necessitates the presence of chiral edge states [3], which in turn imply that zero energy modes can be localised at the core of vortices [4]. Due to particle-hole symmetry these $E = 0$ modes satisfy $\Psi_0^\dagger = \Psi_0$, i.e. they describe excitations that are their own anti-particles, known as Majorana zero modes.

Particle-hole symmetry is a natural property of superconducting fermionic systems. To detect whether a given system can support Majorana zero modes is therefore equivalent to detecting the topologically non-trivial nature of the ground state. This can be given in terms of a topological quantum number ν , the Chern number, that takes integer values [5]. All systems with non-zero ν have chiral edge states, but only systems characterised by odd ν support localised Majorana modes [6]. However, the detection of the Chern number is challenging due to its

non-local nature. Examples exist where this topological invariant is directly related to physical observables, such as the off-diagonal conductivity in the quantum Hall effect [7], but in other microscopically distinct systems such connections are in general unknown.

In this work we show how to robustly measure the Chern number of a superfluid of fermionic atoms from time-of-flight images [8, 9]. We demonstrate our detection method in the context of an experimentally tractable superconducting model that is adiabatically connected to Kitaev's honeycomb lattice [6]. The model supports phases with Chern numbers $\nu = 0, \pm 1$ and ± 2 . The $\nu = \pm 2$ phase emerges uniquely as the collective state of a lattice of Majorana fermions [20]. Thus, the experimental preparation and detection of these phases constitutes two types of direct evidence for the existence of Majorana modes: (i) detecting $\nu = \pm 1$ phases identifies that localised Majorana modes *can be supported* in the system, while (ii) detecting the $\nu = \pm 2$ phases is an unambiguous signature that Majorana modes *do exist* in the system. We show that both the simulation of the superconducting model and the required time-of-flight measurements can be robustly implemented in state-of-the-art ultracold atom experiments [10–12].

Chiral topological order with s -wave pairing:– The realisation of stable p -wave pairing, the usual route for Majorana modes in superconducting systems [5], has been found to be challenging with cold atoms [13]. As an alternative, various routes of combining an effective spin-orbit coupling together with s -wave pairing have been proposed [14, 15]. All these proposals rely on synthesising the spin-orbit coupling using multiple atomic internal states. Here we show that qualitatively similar spin-orbit

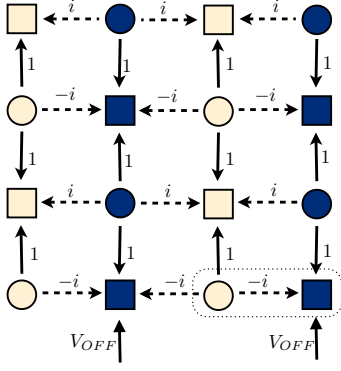


FIG. 1: A chiral topological superconductor with s -wave pairing on a square lattice. When tunnelling of constant magnitude $|t|$ is along the arrows, the numbers denote the complex tunnelling phases. This pattern can be achieved by employing Raman assisted tunnelling with a different set of beams for each direction. The pairing is between neighbouring atoms in two distinct internal states, denoted here as circles and squares, which facilitates the experimental implementation of a real uniform pairing of magnitude Δ . Black (white) columns denote lattice sites with chemical potential $\mu_b = \mu + \delta$ ($\mu_w = \mu - \delta$), where the detuning δ is controlled by a columnwise energy offset V_{OFF} . This overall coupling pattern is translationally invariant with respect to a two site cell containing a black and a white site.

physics can be achieved with a single atomic state by suitably braking translational symmetry.

Our model is defined for fermions on a square lattice and combines staggered complex hopping with a uniform superconducting s -wave interaction. The Hamiltonian is given by

$$H = \sum_{\mathbf{j}} \left[\mu_{\mathbf{j}} a_{\mathbf{j}}^{\dagger} a_{\mathbf{j}} + it(-1)^{j_x} a_{\mathbf{j}}^{\dagger} a_{\mathbf{j}+\hat{x}} + ta_{\mathbf{j}}^{\dagger} a_{\mathbf{j}+\hat{y}} + \Delta(a_{\mathbf{j}}^{\dagger} a_{\mathbf{j}+\hat{x}} + a_{\mathbf{j}}^{\dagger} a_{\mathbf{j}+\hat{y}}) \right] + \text{H.c.}, \quad (1)$$

where $a_{\mathbf{j}}^{\dagger}$ creates a fermion at site $\mathbf{j} = (j_x, j_y)$, the tunnelling amplitude t and pairing potential Δ are both real and the chemical potential $\mu_{\mathbf{j}} = \mu + (-1)^{j_x} \delta$ is staggered by the detuning δ . Translational symmetry is broken along the x -direction with the “magnetic” unit cell (there is no net flux) consisting of a black and a white site, as shown in Fig. 1. Inspired by the Kogut-Susskind fermions [16, 17] we interpret this lattice degree of freedom as a “pseudospin” $\tau \in \{b, w\}$ of the fermions $a_{\tau, \mathbf{j}}$. As detailed in Appendix A, we can thus view the Hamiltonian (1) as an effective pseudospin-orbit coupled system: Tunnelling along the $x(y)$ -direction changes (conserves) the pseudospin state, which effectively realises an anisotropic Rashba type spin-orbit coupling, while the chemical potential detuning plays the role of a Zeeman term. Thus, by adding s -wave pairing, one expects to find Majorana mode supporting topological phases [26].

To verify this, we solve (1) by Fourier trans-

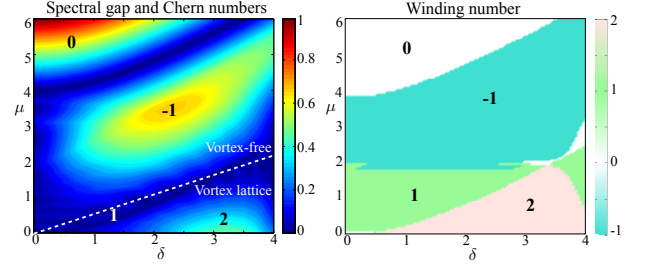


FIG. 2: *Left:* The phase diagram of model (1). Colour encodes the magnitude of the fermionic spectral gap, as a function of the overall chemical potential μ and the detuning δ . The Chern number ν for each phase is shown. The phase diagram is fully symmetric with respect to $\mu \rightarrow -\mu$, while for $\delta \rightarrow -\delta$ all the Chern numbers become time reversed ($\nu \rightarrow -\nu$). As shown in Appendix D, the regions $\mu \lesssim \delta/2$ ($\mu \gtrsim \delta/2$) can be identified with the honeycomb model in the presence (absence) of a vortex lattice. *Right:* The winding number $\tilde{\nu}$ (encoded in colour), as obtained from the observables (5), shows excellent agreement with the Chern numbers ν . The plots are for $t = 1$ and $\Delta = 2$.

forming it with respect to the magnetic unit cell. Writing it subsequently in the particle-hole basis $\psi_{\mathbf{p}}^{\dagger} = (a_{b, \mathbf{p}}^{\dagger}, a_{w, \mathbf{p}}^{\dagger}, a_{b, -\mathbf{p}}, a_{w, -\mathbf{p}})$, we obtain the quadratic Bogoliubov-de Gennes (BdG) Hamiltonian

$$H = \int_{\text{BZ}} \psi_{\mathbf{p}}^{\dagger} H(\mathbf{p}) \psi_{\mathbf{p}} d^2 p, \quad (2)$$

where the Brillouin zone (BZ) spans $p_x \in [0, \pi]$ and $p_y \in [0, 2\pi]$ and the Bloch Hamiltonian $H(\mathbf{p})$ is a 4×4 matrix. The analytic solution to the model is presented in Appendix A. Fig. 2 depicts the phase diagram, which shows that by varying the chemical potentials we can move between a variety of chiral topological phases with Chern number $\nu = 0, \pm 1$ and ± 2 . Each phase is supported by a large range of parameters, thus facilitating its experimental realisation.

As we explicitly show in Appendix B, our model is adiabatically connected to Kitaev’s honeycomb model [6], where chemical potential staggering can be related to the presence of a background vortex lattice. This connection implies that in the non-Abelian $\nu = \pm 1$ phases (in the weakly staggered $\mu \gtrsim \delta/2$ regimes) isolated vortices will bind localised Majorana modes with short range interactions [27]. However, when these vortices form a regular array (the strongly staggered $\mu \lesssim \delta/2$ regime [19]), the interactions cause the Majorana modes to hybridise, which has been shown to lead to a unique collective Abelian state with $\nu = \pm 2$ [20]. Therefore, by simply tuning the chemical potential detuning we can move between regions with and without underlying vortices. Observing the corresponding changes in Chern number provides thus direct evidence for the presence of Majorana modes through their collective behaviour.

Optical lattice implementation:— To physically realise

(1) we suggest to use two interpenetrated 2D optical square lattices. Each lattice hosts a different internal state of the same species of neutral fermionic atoms denoted in Fig. 1 by circles and squares. The lattice is deep enough to suppress ordinary hopping along all three spatial directions. Confinement along the z -direction is taken to be even deeper, so that each xy -plane can be regarded as an independent copy of the same experiment. A Feshbach resonance activates the s -wave pairing [14, 21] between atoms in different internal states, using the fact that the spacing between sublattices is smaller than the separation between atoms in the same state. Hopping between sublattices is achieved by Raman-assisted tunnelling [22–24], a technique that allows both for complex tunnelling amplitudes and also for a delicate control of the chemical potentials [see Appendix C]. The hopping parameter structure can be implemented by means of an energy offset, V_{OFF} , in alternate columns. Note that the complexity introduced by having two species copes with the fact that it is difficult to achieve a Feshbach induced s -wave pairing with atoms in the same state. Should the experiment allow for a same-species Feshbach coupling, the whole setup could be simplified using just a single lattice and the flux inducing mechanism from Ref. [25].

Observables for the Chern number:— We now show how to construct a quantity that (i) is an integer, (ii) is defined in terms of measurable quantities and (iii) reproduces the Chern number in the zero temperature limit. Formally, the Chern number, ν , is defined as the winding number of the projector onto the ground state [7]. When the Bloch Hamiltonian is a 2×2 matrix, i.e. the system is fully translationally invariant, it can always be written as $H(\mathbf{p}) \propto \mathbf{S}(\mathbf{p}) \cdot \boldsymbol{\sigma}$ for some vector field $\mathbf{S}(\mathbf{p})$. Here $\boldsymbol{\sigma}$ denotes a vector of Pauli matrices. The Chern number, ν , is then equivalent to the winding number

$$\tilde{\nu}[\mathbf{S}] = \frac{1}{4\pi} \int_{BZ} \frac{\mathbf{S}(\mathbf{p})}{|\mathbf{S}(\mathbf{p})|^3} \cdot \left(\frac{\partial \mathbf{S}(\mathbf{p})}{\partial p_x} \times \frac{\partial \mathbf{S}(\mathbf{p})}{\partial p_y} \right) d^2p \in \mathbb{Z}, \quad (3)$$

which counts how many times $\mathbf{S}(\mathbf{p})$ winds around the Bloch sphere in the particle-hole space as one spans the whole Brillouin zone [7]. We can obtain this quantity from the components of the vector field $\mathbf{S}(\mathbf{p})$. These components are observables that can be obtained as the ground state expectation values

$$\mathbf{S}(\mathbf{p}) = \langle \Psi | \boldsymbol{\Sigma}_{\mathbf{p}} | \Psi \rangle, \quad \boldsymbol{\Sigma}_{\mathbf{p}} = \boldsymbol{\psi}_{\mathbf{p}}^\dagger \boldsymbol{\sigma} \boldsymbol{\psi}_{\mathbf{p}}, \quad (4)$$

with the physical observables $\boldsymbol{\Sigma}_{\mathbf{p}}$ being given in the basis $\boldsymbol{\psi}_{\mathbf{p}}^\dagger = (a_{\mathbf{p}}^\dagger, a_{-\mathbf{p}})$ of the Bloch Hamiltonian $H(\mathbf{p})$.

To generalize the observable (4) to staggered systems with m site unit cells, we define an independent vector field $\mathbf{S}_{(i)}(\mathbf{p}) = \langle \Psi | \boldsymbol{\Sigma}_{(i),\mathbf{p}} | \Psi \rangle$ for each of the $i = 1, \dots, m$ sublattices. When the full $2m \times 2m$ Bloch Hamiltonian is given in the basis

$\boldsymbol{\psi}_{\mathbf{p}}^\dagger = (a_{1,\mathbf{p}}^\dagger, \dots, a_{m,\mathbf{p}}^\dagger, a_{1,-\mathbf{p}}, \dots, a_{m,-\mathbf{p}})$, the corresponding sublattice observables are $\boldsymbol{\Sigma}_{(i),\mathbf{p}} = \boldsymbol{\psi}_{(i),\mathbf{p}}^\dagger \boldsymbol{\sigma} \boldsymbol{\psi}_{(i),\mathbf{p}}$ with $\boldsymbol{\psi}_{(i),\mathbf{p}}^\dagger = (a_{(i),\mathbf{p}}^\dagger, a_{(i),-\mathbf{p}})$. Explicitly, their components are given by

$$\begin{aligned} \Sigma_{(i),\mathbf{p}}^x &= a_{(i),\mathbf{p}}^\dagger a_{(i),-\mathbf{p}}^\dagger + a_{(i),-\mathbf{p}} a_{(i),\mathbf{p}}, \\ \Sigma_{(i),\mathbf{p}}^y &= -i a_{(i),\mathbf{p}}^\dagger a_{(i),-\mathbf{p}}^\dagger + i a_{(i),-\mathbf{p}} a_{(i),\mathbf{p}}, \\ \Sigma_{(i),\mathbf{p}}^z &= a_{(i),\mathbf{p}}^\dagger a_{(i),\mathbf{p}} - a_{(i),-\mathbf{p}} a_{(i),-\mathbf{p}}^\dagger. \end{aligned} \quad (5)$$

Substituting these into (4), we can construct m winding numbers $\tilde{\nu}_{(i)} = \tilde{\nu}[\mathbf{S}_{(i)}]$, $i = 1, \dots, m$. We now define the total winding number by

$$\tilde{\nu} = \sum_{i=1}^m \tilde{\nu}_{(i)}. \quad (6)$$

By direct comparison we observe that, for the case of the two site staggered model (1), the winding number $\tilde{\nu}$ is in excellent agreement with the Chern number ν for all coupling regimes, as shown in Fig. 2. In particular, phases with different $|\nu|$ are exactly distinguished, so the observables $\boldsymbol{\Sigma}_{b,\mathbf{p}}$ and $\boldsymbol{\Sigma}_{w,\mathbf{p}}$ can be used to faithfully identify the topological phases of our model [see Appendix D].

The experimental measurement of $\boldsymbol{\Sigma}_{(i),\mathbf{p}}$ proceeds in several steps. Time-of-flight images give direct access to $\langle a_{(i),\mathbf{p}}^\dagger a_{(i),\mathbf{p}} \rangle$, for both $i = b, w$ separately, which is enough to obtain S^z . To obtain the orthogonal components S^x and S^y , we note that pairing in the Hamiltonian (1) along the y -direction is proportional to the operator Σ^y . An evolution under only this term implements a rotation around the S^y axis, which maps the value S^x onto the measurable S^z . Thus, to measure S^x , we suggest first applying this rotation for a brief period of time, for instance by ramping up the optical lattice along the x -direction and switching off the hopping, and only then performing the time-of-flight measurement. While the setup contains no similar rotation to map S^y to S^z , it can be obtained from noise correlation measurements once both S^x and S^z are known [see Appendix D]. As the time of flight images are digitalised one could either compute the discretised version of (3) [9] or perform a continuous fit to the values of S^x , S^y and S^z .

Robustness to experimental errors:— Our measurement procedure is robust under the two main cold atom experiment imperfections – a harmonic trapping potential and a finite temperature. We simulate the first in a finite $L \times L$ system with open boundary conditions by introducing in (1) the chemical potential $\mu_{\mathbf{j}} = \mu + (-1)^{j_x} \delta + M d^2 \omega^2 [(j_x - L/2)^2 + (j_y - L/2)^2]$, where M is the mass of the atomic species and d is the lattice spacing. Such a potential removes the idealised conditions of translational symmetry that is required for the formal definition of the Chern number. Assuming that a local density approximation holds, this spatially dependent chemical potential induces the coexistence of different phases: some of insulating character, some not;

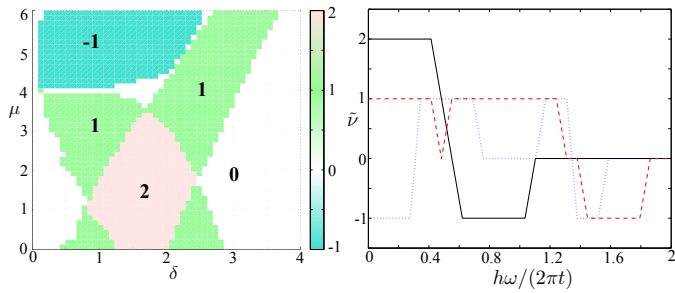


FIG. 3: The effect of a harmonic trap for the atoms on the winding number $\tilde{\nu}$. *Left*: Winding number $\tilde{\nu}$ (encoded in colour) as measured by the observables (4) in a 15×15 lattice with a trapping frequency $\hbar\omega/t = 0.5$. *Right*: The winding numbers as the trapping frequency ω is increased for the $\nu = 2$ phase $(\delta, \mu) = (3, 0)$, [black solid line], the $\nu = 1$ phase $(\delta, \mu) = (4, 2)$, [red dashed line] and the $\nu = -1$ phase $(\delta, \mu) = (1, 3)$, [blue dotted line]. Both figures assume a lattice spacing of 500nm and the atomic mass of ^{40}K .

some with topological order, some with no order at all. Nevertheless, our time-of-flight images will suppress the contribution from all trivial phases.

Comparison between Fig. 2 and Fig. 3 shows that while the phase diagram is deformed, all the topological phases, as characterised by the winding number $\tilde{\nu}$, remain robust for an extended range of trapping frequencies ω . Since the same winding number reproduced the Chern numbers in the idealised unperturbed system, we regard that it faithfully capturing the nature of the topological order also in perturbed systems.

To model the effect of finite temperature T we restrict to fermionic excitations in the lower band with no thermal vortex excitations. Then the ground state $|\Psi(\mathbf{p})\rangle$ is replaced by a thermal state, which has occupation n_- in the ground state and occupation n_+ in the first excited state. Here $n_{\pm} = 1/(\exp(\pm \frac{E_1(\mathbf{p})}{kT}) + 1)$ is the Fermi distribution for the lowest lying energy band $E_1(\mathbf{p})$. Evaluating the expectation values (4) on this state we find $\mathbf{S}_{(i)} \rightarrow \mathbf{S}_{(i)T} = (n_- - n_+)\mathbf{S}_{(i)}$. This implies that finite temperature only changes the normalisation of the vector fields. Thus, the winding number (3) still faithfully reproduces the Chern number. The decrease in the visibility $|\mathbf{S}_{(i)T}|^2$ means that the time-of-flight measurements become more susceptible to noise, but this can be compensated by sufficient experimental precision. This contrasts with the behaviour of topological entanglement entropy, which provides an alternative probe for topological order in cold atom systems [28]. In the thermodynamic limit topological entropy vanishes at any finite temperature rendering its applicability challenging [29]. Furthermore, unlike our method, topological entropy can not distinguish topological phases with same total quantum dimensions [2].

Conclusions:— We have presented a general method to detect the Chern number of superconducting mod-

els from time-of-flight images. We showed that our method can detect phases with Chern numbers $\nu = \pm 1$ or $\nu = \pm 2$, thereby identifying those that can support localised Majorana zero modes or arise through their collective behaviour, respectively. Both types of phases arise in the proposed model, which establishes a new route to topological phases with cold atoms. Staggered tunnellings of spinless fermions realise an effective spin-orbit coupling, which, in analogy to topological semiconductor heterostructures [26], can give rise to Majorana modes when s -wave pairing is introduced. We showed this explicitly by adiabatically connecting the staggered model to Kitaev's honeycomb model [6], where both the properties of the non-Abelian vortices in the $\nu = \pm 1$ phases [27] and their collective behaviour [20] has been extensively studied. While we demonstrated our experimentally robust measurement scheme in the context of a particular model, our method is readily applicable also to other cold atom realisations of topological phases [14, 15]. An important open question is the interplay between different phases in an experiment with inhomogeneities, where the boundaries are not so clearly defined.

Acknowledgements:— JKP would like to thank Wolfgang Ketterle for inspiring conversations. This work was supported by EPSRC and by Spanish MICINN Project FIS2009-10061, FPU grant No.AP 2009-1761, CAM research consortium QITEMAD S2009-ESP-1594.

-
- [1] E. Majorana, *Nuovo Cimento*, **5**, 171 (1937).
 - [2] J. K. Pachos, *Introduction to Topological Quantum Computation*, Cambridge University Press (2012).
 - [3] Y. Hatsugai, *Phys. Rev. Lett.* **71**, 3697 (1993).
 - [4] C. Chamon *et al.*, *Phys. Rev. B* **81**, 224515 (2010).
 - [5] N. Read and D. Green, *Phys. Rev. B* **61**, 10267 (2000).
 - [6] A. Kitaev, *Ann. Phys.* **321**, 2 (2006).
 - [7] D. J. Thouless, *et al.*, *Phys. Rev. Lett.* **49**, 405 (1982).
 - [8] E. Zhao, N. Bray-Ali, C. J. Williams, I. B. Spielman and I. I. Satija, *Phys. Rev. A* **84**, 063629 (2011).
 - [9] E. Alba *et al.*, *Phys. Rev. Lett.* **107**, 235301 (2011).
 - [10] E. Altman, E. Demler and M. D. Lukin, *Phys. Rev. A* **70**, 013603 (2004).
 - [11] S. Fölling *et al.*, *Nature* **434**, 481 (2005).
 - [12] M. Greiner, *et al.*, *Phys. Rev. Lett.* **94**, 110401 (2005).
 - [13] J. P. Gaebler, *et al.*, *Phys. Rev. Lett.* **98**, 200403 (2007).
 - [14] L. Jiang *et al.*, *Phys. Rev. Lett.* **106**, 22 (2011).
 - [15] C. Zhang, *et al.*, *Phys. Rev. Lett.* **101**, 160401 (2008); C. Zhang, *Phys. Rev. A*, **82**, 021607 (2010); S. Zhu *et al.*, *Phys. Rev. Lett.* **106**, 100404 (2011).
 - [16] P. Maraner and J. K. Pachos, *Phys. Lett. A* **373**, 2542 (2009).
 - [17] J. B. Kogut, and L. Susskind, *Phys. Rev. D* **11**, 395 (1975); L. Susskind, *Phys. Rev. D* **16**, 3031 (1977).
 - [18] D. A. Ivanov, *Phys. Rev. Lett.* **86**, 268 (2001).
 - [19] V. Lahtinen and J.K. Pachos, *Phys. Rev. B* **81**, 245132 (2010); J. K. Pachos, *Ann. Phys.* **322**, 1254 (2007).
 - [20] V. Lahtinen, *et al.*, *Phys. Rev. B* **86**, 075115 (2012).
 - [21] G. M. Bruun and C. J. Pethick, *Phys. Rev. Lett.* **92**, 14

- (2004).
- [22] D. Jaksch and P. Zoller, New J. Phys. **5**, 56 (2003).
- [23] F. Gerbier and J. Dalibard, New J. Phys. **12**, 033007 (2010).
- [24] L. Mazza *et al.*, New J. Phys. **14**, 015007 (2012).
- [25] M. Aidelsburger *et al.*, Phys. Rev. Lett. **107**, 255301 (2011).
- [26] J. Alicea, Phys. Rev. B **81**, 125318 (2010).
- [27] V. Lahtinen, New J. Phys. **13**, 075009 (2011).
- [28] D.A. Abanin and E. Demler, Phys. Rev. Lett. **109**, 020504 (2012).
- [29] C. Castelnovo and C. Chamon, Phys. Rev. B **76**, 184442 (2007); S. Iblisdir, D. Perez-Garcia, M. Aguado and J.K. Pachos, Phys. Rev. B **79**, 134303 (2009).

Appendix A: Chiral topological order with s -wave pairing

In this Appendix we first give the analytic solution to our model (1) and then discuss its interpretation as an effective spin-orbit coupled system with s -wave pairing. We also show how sign staggered couplings in a p -wave model allow for the complex pairing to be traded for real s -wave pairing with complex hopping.

Analytic solution

The Hamiltonian (1) can be Fourier transformed with respect to the magnetic unit cell. Writing it in the particle-hole basis $\psi_{\mathbf{p}}^{\dagger} = (a_{b,\mathbf{p}}^{\dagger}, a_{w,\mathbf{p}}^{\dagger}, a_{b,-\mathbf{p}}, a_{w,-\mathbf{p}})$, we obtain the quadratic Bogoliubov-de Gennes Hamiltonian $H = \int_{BZ} \psi_{\mathbf{p}}^{\dagger} H(\mathbf{p}) \psi_{\mathbf{p}} d^2p$, where

$$H(\mathbf{p}) = \begin{pmatrix} f_+ & ig_+^* & ih & g_-^* \\ -ig_+ & f_- & -g_- & ih \\ -ih & -g_-^* & -f_+ & ig_+^* \\ g_- & -ih & -ig_+ & -f_- \end{pmatrix}, \quad (7)$$

with

$$\begin{aligned} f_{\pm} &= (\mu \pm \delta) + 2t \cos(p_y), \\ g_+ &= t(1 + e^{2ip_x}), \\ g_- &= \Delta(1 - e^{2ip_x}), \\ h &= 2\Delta \sin(p_y). \end{aligned}$$

By employing a Bogoliubov transformation

$$b_{n,\mathbf{p}} = \sum_{i \in (b,w)} (u_{ni} a_{(i),\mathbf{p}}^{\dagger} + v_{ni} a_{(i),-\mathbf{p}}),$$

for some complex coefficients u_{ni} and v_{ni} , the Hamiltonian can be brought to the diagonal form

$$H = \sum_{n=1,2} \int_{BZ} d^2p \left[E_n^+(\mathbf{p}) b_{n,\mathbf{p}}^{\dagger} b_{n,\mathbf{p}} + E_n^-(\mathbf{p}) b_{n,-\mathbf{p}} b_{n,-\mathbf{p}}^{\dagger} \right].$$

The four energy bands are given by

$$E_n^{\pm}(\mathbf{p}) = \pm \sqrt{A(\mathbf{p}) + (-1)^n \sqrt{A^2(\mathbf{p}) - 4B(\mathbf{p})}}, \quad (8)$$

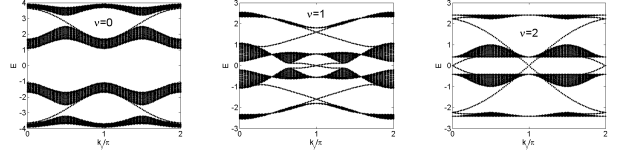


FIG. 4: The spectral flow on a cylinder for the $\nu = 0$ ($\mu = 0, \delta = 5$), $\nu = 1$ ($\mu = 2, \delta = 5$) and $\nu = 2$ ($\mu = 0, \delta = 2$) phases showing $|\nu|$ edge states crossing zero energy per edge. The plots are for $t = \Delta = 1$.

where

$$\begin{aligned} A(\mathbf{p}) &= f_+^2 + f_-^2 + 4(|g_+|^2 + h^2 + |g_-|^2), \\ B(\mathbf{p}) &= |g_+|^4 + h^4 + |g_-|^4 + f_+^2 f_-^2 + \\ &\quad h^2(f_+^2 + f_-^2) - 2f_+ f_- (|g_+|^2 - |g_-|^2) - \\ &\quad 2h^2(|g_+|^2 + |g_-|^2) - 2\text{Re}(g_- g_+^*)^2. \end{aligned}$$

The particle-hole symmetry present in the problem is represented by $C = \sigma^x \otimes \mathbb{1}$ that swaps the creation and annihilation operators of opposite momenta. It acts on (7) as $CH(\mathbf{p})C^{-1} = -H^*(-\mathbf{p})$, which implies that zero energy eigenstates at the momenta $\mathbf{p} = (0, 0), (0, \pi)$ will be self-conjugate. Fig. 4 shows that the edge states indeed cross zero energy at these momenta implying that they are (dispersing) Majorana modes. In the presence of a vortex (a puncture in the plane with π -flux through it), the edge states will become localised Majorana modes [4]. Odd number of edge states implies that an isolated Majorana mode will always remain localised at zero energy at the vortex core, while an even number of them leads to complete hybridisation with all the Majorana modes pairing up to localised Dirac fermions.

Staggered tunnelling as an effective spin-orbit coupling

Even if there is no net magnetic field through the system, staggering in the couplings leads to an enlarged unit cell. For the coupling pattern shown in Fig. 1, the unit cell consists of two sites, which we denote as black (b) and white (w). Interpreting this lattice degree of freedom as a pseudospin $\tau \in (b, w)$ of the fermions $a_{\mathbf{j},\tau}^{\dagger}$, using the “spinor” $\psi_{\mathbf{j}}^{\dagger} = (a_{b,\mathbf{j}}^{\dagger}, a_{w,\mathbf{j}}^{\dagger})$ we can rewrite the different terms of (1) in the following way:

$$\begin{aligned} \mu_{\mathbf{j}} a_{\mathbf{j}}^{\dagger} a_{\mathbf{j}} &\rightarrow \mu \psi_{\mathbf{j}}^{\dagger} \psi_{\mathbf{j}} + V_z \psi_{\mathbf{j}}^{\dagger} \tau^z \psi_{\mathbf{j}}, \\ i(-1)^{j_x} t a_{\mathbf{j}+\hat{x}}^{\dagger} a_{\mathbf{j}} &\rightarrow \alpha \psi_{\mathbf{j}}^{\dagger} \tau^y \psi_{\mathbf{j}+\hat{x}} + V_y \psi_{\mathbf{j}}^{\dagger} \tau^y \psi_{\mathbf{j}}, \\ t a_{\mathbf{j}+\hat{y}}^{\dagger} a_{\mathbf{j}} &\rightarrow t \psi_{\mathbf{j}}^{\dagger} \psi_{\mathbf{j}+\hat{y}}, \\ \Delta a_{\mathbf{j}+\hat{x}}^{\dagger} a_{\mathbf{j}} &\rightarrow \Delta \psi_{\mathbf{j}}^{\dagger} \tau^x \psi_{\mathbf{j}+\hat{x}}, \\ \Delta a_{\mathbf{j}+\hat{y}}^{\dagger} a_{\mathbf{j}} &\rightarrow \Delta \psi_{\mathbf{j}}^{\dagger} \psi_{\mathbf{j}+\hat{y}}, \end{aligned} \quad (9)$$

where the Pauli matrices τ^{α} act on the pseudospin degree of freedom. This suggests the following interpretation in terms of the fermions $\psi_{\mathbf{j}}^{\dagger}$:

- μ still acts as the chemical potential, while the detuning acts now effectively as a Zeeman term of magnitude $V_z = \delta$.
- Tunnelling in x -direction realizes an anisotropic Rashba type spin-orbit coupling $p_x \sigma^y$ of magnitude $\alpha = t$ and a transverse magnetic field of magnitude $V_y = t$.
- Pairing will be of uniform amplitude Δ , but it will be an anisotropic mixture of singlet (x -direction) and triplet pairing (y -direction).

The elements above – the spin-orbit coupling, magnetic fields of different direction and the s -wave pairing – are the components of Majorana mode hosting semiconductor heterostructures [26].

These components appear also in a staggered p -wave superconductor, where, similar to our model, the staggering allows complex pairing to be traded for complex hopping. Denoting the fermionic operators a_j^\dagger by b_j^\dagger (w_j^\dagger) when they live on the black (white) sublattice, shown in Fig. 1, we can write the simplest possible p -wave lattice model as [1]

$$H_{p_x+ip_y}^u = \sum_j \left[\left(\mu_+ b_j^\dagger b_j + \mu_- w_j^\dagger w_j \right) + t \left(u b_j^\dagger b_{j+\hat{y}} + w_j^\dagger w_{j+\hat{y}} + i b_j^\dagger w_j - i w_j^\dagger b_{j+\hat{x}} \right) + \Delta \left(-u b_j^\dagger b_{j+\hat{y}}^\dagger + w_j^\dagger w_{j+\hat{y}}^\dagger + b_j^\dagger w_j^\dagger + w_j^\dagger b_{j+\hat{x}}^\dagger \right) \right], \quad (10)$$

where $\mu_\pm = \mu \pm \delta$, t and Δ are again the tunnelling amplitude and the pairing potential, respectively. To stagger the couplings, we have introduced the parameter u . While $u = 1$ recovers the original Hamiltonian of [1] (up to a unitary $b_j^\dagger \rightarrow i b_j^\dagger$ and subsequently identifying $b_j = w_j$), setting $u = -1$ breaks translational symmetry by flipping the signs of the tunnelling and pairing on the black sites. This results in the pairing becoming real and uniform s -wave pairing, while the complex p -wave symmetry is transferred to the tunnelling amplitudes. In addition, the sublattice dependent sign staggered tunnelling in the y -direction means that we have introduced π -flux on each square plaquette. Fourier transformation gives a Hamiltonian of the form (7) with the only difference that one needs to replace $f_+ \rightarrow f_+^u = (\mu + \delta) + 2ut \cos(p_y)$. Diagonalisation gives a phase diagram that under swapping $\mu \leftrightarrow \delta$ is identical to that of Fig. 2. Staggering enables thus to trade complex pairing into complex hopping (with or without net magnetic field), while preserving topologically non-triviality the phase diagram. This can be advantageous from the point of view of experiments where complex tunnelling is in general easier to realise than a complex pairing.

Writing (10) in terms of the spinor $\psi_j^\dagger = (b_j^\dagger, w_j^\dagger)$, we obtain a similar interpretation of the Hamiltonian describing a pseudospin-orbit coupled system. The only difference to (9) is that the sublattice dependent tunnelling

in y -direction gives rise to a further spin-orbit term of Dresselhaus type ($\psi_j^\dagger \tau^z \psi_{j+\hat{y}}$). Borrowing from the behaviour of the topological heterostructures [26], this extra term enables us to gain insight into the swapped behaviour of the models when tuning μ and δ . There it is known that in the presence of only Rashba coupling, i.e. in the original model (1), a finite perpendicular Zeeman field $V_z = \delta$ is required to drive the system into a topological phase. On the other hand, when a Dresselhaus coupling is present, an in-plane magnetic field $V_y = t$ is sufficient. Indeed, the model (10) above has topological phases even for $\delta = 0$.

Appendix B: Adiabatic connection to Kitaev's honeycomb lattice model

In this Appendix we demonstrate that our staggered model (1) is adiabatically connected to Kitaev's honeycomb model [6]. We show this explicitly for the $\nu = \pm 2$ phases that arise in the full-vortex sector of the model [19] due to the collective behaviour of the Majorana modes bound at the vortex cores [20].

The honeycomb model is a local spin lattice model that can be adiabatically connected to the $p_x + ip_y$ superconductor [2]. It can be solved exactly by mapping it to a tight-binding model of free Majorana fermions on the honeycomb lattice with nearest (magnitudes J_x, J_y and J_z depending on link orientations) and next nearest neighbour (magnitude K) tunnelling [6]. After this mapping, the Hamiltonian in the full-vortex sector (π -flux on each hexagonal plaquette) can be written as [3, 19]

$$H_{f.v.} = i \sum_j [(-1)^{j_x} J_z a_j b_j + J_x a_j b_{j+\hat{x}} + J_y a_j b_{j+\hat{y}}] + iK \sum_j (-1)^{j_x} [a_j a_{j-\hat{x}} + a_j a_{j+\hat{y}} + b_j b_{j+\hat{x}} + b_j b_{j-\hat{y}}], \quad (11)$$

+ H.c.

where $a_j^\dagger = a_j$ and $b_j^\dagger = b_j$ are Majorana operators on the two triangular sublattices of the honeycomb lattice. To simplify the model we have included only four out of the six possible next nearest neighbour hoppings (the omitted terms being $a_j a_{j+\hat{x}+\hat{y}}$ and $b_j b_{j+\hat{x}+\hat{y}}$).

The full-vortex sector is encoded in the $(-1)^{j_x}$ factors that stagger the signs of the Majorana hopping amplitudes J_z and K . Pairing the Majorana operators into complex fermions c_j by

$$a_j = e^{i\theta_j} c_j + e^{-i\theta_j} c_j^\dagger, \quad b_j = \frac{1}{i} (e^{i\theta_j} c_j - e^{-i\theta_j} c_j^\dagger), \quad (12)$$

(the phase θ_j to be defined below) the links connecting the a_j and b_j sites of the honeycomb lattice become the sites of a square lattice. In this basis the Hamiltonian

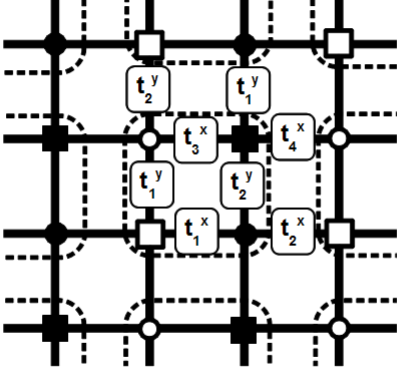


FIG. 5: When the Majorana operators a_j and b_j are paired into complex fermions c_j , the links connecting them become sites of the square lattice. The resulting Hamiltonian with couplings (14) has a four site unit cell shown here as the dashed boxes. Redefining the operators on the circle (square) sites by $c_j \rightarrow e^{i\chi} c_j$ ($c_j \rightarrow e^{-i\chi} c_j$) preserves the real pairing for arbitrary χ while unitarily transforming the hopping amplitudes. For $\chi = \phi/2 - \pi/4$ they are brought to the form (15). The chemical potential μ_j alternates in the x -direction between $2J_z$ (black sites) and $-2J_z$ (white sites).

takes the BCS form

$$H_{f.v.} = \sum_j [\mu_j c_j^\dagger c_j + t_j^x c_j^\dagger c_{j+\hat{x}} + t_j^y c_j^\dagger c_{j+\hat{y}} + \Delta_x c_j c_{j+\hat{x}} + \Delta_y c_j c_{j+\hat{y}}] + \text{H.c.}, \quad (13)$$

where we defined

$$\begin{aligned} \mu_j &= 2J_z(-1)^{j_x} \\ t_j^x &= r e^{i(-1)^{j_x}(2-(-1)^{j_y})\phi}, \\ t_j^y &= 2J e^{-i(-1)^{j_x+j_y}\phi}, \\ \Delta_x &= 2J, \\ \Delta_y &= r, \end{aligned} \quad (14)$$

with $J = J_x = J_y$, $r = \sqrt{(2J)^2 + (4K)^2}$ and $\phi = \arctan(J/(2K))$. In terms of these variables the phase in (12) is given by $\theta_j = -(-1)^{j_x} \frac{1-(-1)^{j_y}}{2} \phi$.

The variables t_j^x , t_j^y , r and ϕ are all functions of the honeycomb couplings J , J_z and K . From now on we will treat them as independent variables and show that (13) can be adiabatically connected to (1). First of all, we set the scale by directly identify the chemical potential detuning to be $\delta = 2J_z$ with the overall chemical potential set to $\mu = 0$. Next, we would like to tune $r \rightarrow 2J \equiv t$ in order to make the tunnelling and pairing amplitudes equal. Fig. 6 shows that the gap increasing during this process. Finally, we would like to tune the phase of the tunnelling amplitudes (14). As illustrated in Fig. 5, these couplings are translationally invariant with respect to a

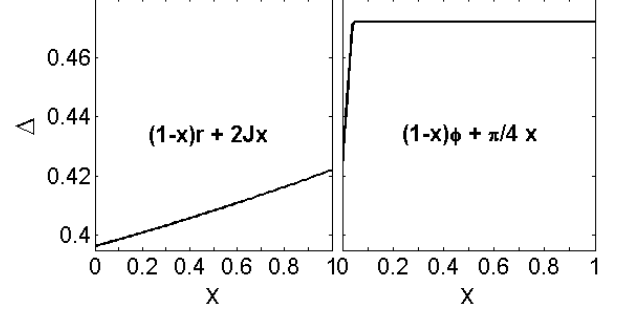


FIG. 6: Adiabatic connection between the $\nu = -2$ phases in the full-vortex sector of the honeycomb model and in (1). *Left:* As we first tune $r \rightarrow 2J$ for the tunnelling couplings $t_i^{x,y}$ and the pairing potentials Δ_α to have equal amplitudes, the gap Δ increases. *Right:* Tuning subsequently $\phi \rightarrow \pi/4$ to match the phase pattern in the hoppings, we find the gap first increasing and then settling to a constant value. The data is for $J = J_z = 1$ and $K = 0.1$. Both transitions are performed with a linear ramp parameterised by $x \in [0, 1]$.

four site unit cell and there are altogether six independent tunnelling couplings for a general ϕ . These can be unitarily transformed to the form

$$\begin{aligned} t_1^x &= t e^{i\pi/2} \rightarrow it, \\ t_2^x &= t e^{-i\pi/2} \rightarrow -it, \\ t_3^x &= t e^{4i\phi - i\pi/2} \rightarrow it, \\ t_4^x &= t e^{-4i\phi + i\pi/2} \rightarrow -it, \\ t_1^y &= t e^{-2i\phi + i\pi/2} \rightarrow t, \\ t_2^y &= t e^{2i\phi - i\pi/2} \rightarrow t, \end{aligned} \quad (15)$$

and subsequently tuned to the special value $\phi = \pi/4$ (the \rightarrow above), which gives a two site unit cell with the same tunnelling phases as in the staggered model (1). Fig. 6 shows the gap remains non-zero during this process, which implies that the models are adiabatically connected. Indeed, for $J = J_z = 1$ and $K > 0$ the honeycomb model is in a nucleated $\nu = -2$ phase [19]. These honeycomb couplings correspond to $t = \Delta_x = \Delta_y = -\delta = 2$ and $\mu = 0$ for which, as shown in Fig. 2, we also find a $\nu = -2$ (the chemical potential detuning δ is here negative).

A remarks is in order. Since we put the sign staggering in (11) on the couplings J_z and subsequently paired the Majoranas along these links, the resulting square lattice model has a staggered chemical potential, but no flux per plaquette (one can verify that the phases in the tunnellings (14) cancel). This is basis dependent though. Had we paired the Majoranas along, say, J_y couplings, we would have arrived at a model with a uniform chemical potential and π -flux per plaquette. This shows that there is nothing special about having a real magnetic field in the system – it is the staggering that encodes the physics.

The full phase diagram of the full-vortex sector of the

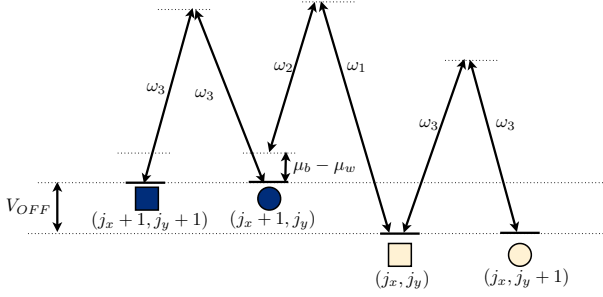


FIG. 7: Energy level structure, showing how two sets of Raman beams allow for independent transitions due to the presence of the offset V_{OFF} . This offset can be tuned to allow for different values of the difference in chemical potentials $\mu_w - \mu_b$. The indices (j_x, j_y) stand for horizontal and vertical position on the lattice, respectively.

honeycomb model has been studied in [19]. We can employ it to understand some of the features of the phase diagram of Fig. 2. First of all, in the dimerised limits $|J_z| \gg |J|$ one always finds a $\nu = 0$ phase, in agreement with us finding $\nu = 0$ phases in both $\delta \gg \mu$ and $\mu \gg \delta$ limits. For intermediate values one is either in a $\nu = \pm 1$ or a $\nu = \pm 2$ depending on the degree of staggering $\delta = 2J_z$. While the honeycomb model has always $\mu = 0$ chemical potential when derived from the spin model, we can introduce a finite μ by hand. Doing so one finds that for $\mu > \delta/2$ the non-Abelian $\nu = \pm 1$ phase is recovered even if some sign staggering remains [19]. This is in agreement with Fig. 2, which shows along the $\mu \approx \delta/2$ line a similar transition between the Abelian $\nu = 2$ and the non-Abelian $\nu = -1$ phases. We thus interpret the region $\mu < \delta/2$ as the one where the collective vortex lattice effects, and those of the Majorana modes bound to them, are relevant. The $\mu > \delta/2$ region, however, should be understood as having similar physics as the vortex-free sector where isolated vortices bind localised Majorana modes.

Appendix C: Optical lattice implementation

We propose to generate the lattice of model (1) by focusing the diffracted image from a holographic mask onto the focal plane of an extremely large aperture lens [4]. The sublattices host different hyperfine states of the same atomic species which are sensitive to different polarisations of the trapping laser beams. Both sublattices can be displaced one on top of another by means of an electro-optic modulator [5].

We also superimpose a superlattice potential $V = V_{OFF} \sin^2(\pi x/2d)$ whose amplitude can be controlled by changing the intensity of the laser beam, which creates this potential. This superlattice structure effectively adds a tunable energy offset V_{OFF} to every other column in the lattice. This offset serves a two-fold purpose: it al-

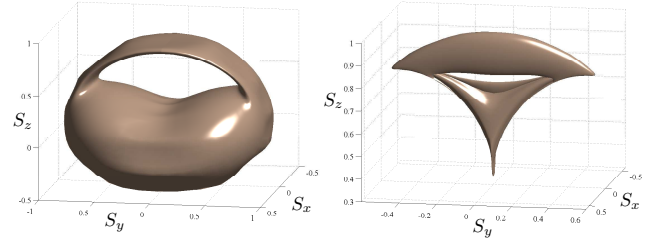


FIG. 8: Illustration of the vector field \mathbf{S} for a $\tilde{\nu} = -1$ phase. Here we plot the values of $\mathbf{S}_{(b)}$ (left) and $\mathbf{S}_{(w)}$ (right) for $(\delta, \mu) = (1, 3)$. It can be seen that $\mathbf{S}_{(b)}$ winds once around the origin, thus giving a partial $|\tilde{\nu}_b| = +1$ contribution, while $\mathbf{S}_{(w)}$ does not enclose the origin so it gives zero contribution.

lows for independent Raman tunnelling in each direction and acts as a knob for changing the value of the chemical potential difference $\mu_w - \mu_b$, as it can be seen in Fig. 7.

Our implementation employs a Raman-assisted tunnelling scheme on an optical lattice with a pattern of phases, as shown in Fig. 1 [22–24]. In this figure we use a convention that the tunnelling direction is set to go from one species (circle) to the other (square). Reversing the direction complex conjugates the tunnelling amplitude. The tunnelling element between sites \mathbf{j} and \mathbf{j}' in a Raman transition assisted by two lasers of wavevectors \mathbf{k}_1 and \mathbf{k}_2 of amplitude V_0 can be parameterised as $t = V_0 e^{i\mathbf{q} \cdot \mathbf{r}_+} t_0(d, \mathbf{q})$, where t_0 is a real number which only depends on the nearest-neighbour distance d and the difference between the Raman beam wavevectors $\mathbf{q} = \mathbf{k}_1 - \mathbf{k}_2$. Also $\mathbf{r}_+ = (\mathbf{j} + \mathbf{j}')/2$ is the midpoint between the two neighbouring sites. The phase of the hopping parameter is thus determined by wavevector \mathbf{q} . We can see in Fig. 1 that two different phase wavelengths for the horizontal and vertical transition amplitudes are needed. So implementation of this hopping pattern requires a Raman pair for each direction. Fig. 7 shows the energy level structure which accomplishes this pattern.

Appendix D: Measurement protocol

To obtain the winding number $\tilde{\nu}$ one needs to first construct the two independent integer-valued winding numbers $\tilde{\nu}_b$ and $\tilde{\nu}_w$. The structure of the observable vector fields $\mathbf{S}_{(b,w)}$ itself also provides valuable information regarding the topology of the system. Fig. 8 shows a 3D-representation of these vector fields in a state with $\tilde{\nu} = -1$. We can see that a non-trivial contribution appears whenever the vector field structure winds around the origin (it is assumed that the vector field is nowhere zero, which is reasonable if the temperature is kept low enough). These diagrams may hint a non-trivial topology of the system even if the winding number cannot be accurately computed due to experimental imperfections.

Our characterisation of the quantum phases is based

on the winding of the vector fields $\mathbf{S}_{(i)}$, which are defined independently for the “black” ($i = b$) and “white” ($i = w$) sublattices distinguished by their different chemical potential. The energy offsets between them can be employed to release atoms from one of the two sublattices at a time, thus obtaining $n_{b,\mathbf{p}}$ and $n_{w,\mathbf{p}}$, and the observable $S_{(i)}^z(\mathbf{p}) = n_{(i),\mathbf{p}} + n_{(i),-\mathbf{p}} - 1$ for both $i = b, w$.

For the components S^x and S^y we suggest employing two complementary techniques. The reason for this is that measuring the transverse components requires momentum-dependent operations and having two different methods allows for a more robust calibration and redundancy in the measurements.

The first method takes the same time-of-flight images which are used for $S_{(i)}^z(\mathbf{p})$ but processes them to obtain the noise correlations, $\langle n_{(i),\mathbf{p}} n_{(i),-\mathbf{p}} \rangle$. Using Wick’s theorem we can show that such an observable can be written in the form

$$\begin{aligned} \langle n_{(i),\mathbf{p}} n_{(i),-\mathbf{p}} \rangle &= \langle n_{(i),\mathbf{p}} \rangle \langle n_{(i),-\mathbf{p}} \rangle + |\langle a_{(i),\mathbf{p}}^\dagger a_{(i),-\mathbf{p}} \rangle|^2 \\ &\quad + \langle a_{(i),\mathbf{p}}^\dagger a_{(i),-\mathbf{p}} \rangle \langle a_{(i),\mathbf{p}} a_{(i),-\mathbf{p}}^\dagger \rangle. \end{aligned} \quad (16)$$

We can eliminate in this equation the values $\langle a_{(i),\mathbf{p}} a_{(i),-\mathbf{p}}^\dagger \rangle$, for they can be obtained from time-of-flight measurements after Bragg scattering with momentum $2\mathbf{p}$; but in addition they are also zero in our setup. This means that in essence noise correlation give us access to the orthogonal projection of the pseudo-spin components, $(S^\perp)^2 = (S^x)^2 + (S^y)^2$.

The second method consists on applying the pairing interactions for a very brief time prior to the time-of-flight images. The Hamiltonian (2), when we switch off the hopping $t = 0$ and leave only the pairing along the y direction, acquires the form

$$H_{rot} = \Delta \sin(p_y) i \left(a_{(i),\mathbf{p}}^\dagger a_{(i),\mathbf{p}}^\dagger - \text{H.c.} \right) \propto \Sigma_{(i),\mathbf{p}}^y. \quad (17)$$

This operator implements a rotation around the S^y axis,

mapping the value of the S^x operator onto the S^z axis

$$S^z(\mathbf{p}, t) = \cos(\theta_{\mathbf{p}}) S^z(\mathbf{p}, 0) + \sin(\theta_{\mathbf{p}}) S^x(\mathbf{p}, 0), \quad (18)$$

with $\theta = \Delta \sin(p_y) t / \hbar$. This allows us to extract the value of S^x , with some difficulties around $p_y = 0, \pm\pi$, to be discussed now.

The value of S^y is implicit in the previous measurements, through the formula, $(S^y)^2 = (S^\perp)^2 - (S^x)^2$. It can also be obtained experimentally using a two-step process. The first part consists on an evolution with hopping along the y direction, that maps S^y to S^x , while the last step uses again the pairing to measure S^x .

In practice, as the rotation angles of the operations mentioned above becomes infinitely slow for $p_y = 0, \pm\pi/2, \pm\pi$, we instead suggest to use a clever fitting procedure, extrapolating smoothly the values of \mathbf{S} from the measurements of S^z, S^x, S^\perp and S^y . From our numerical experiments, this can be done effectively, as the norm of \mathbf{S} does not become zero anywhere, and the angles in the xy plane behave smoothly across the Brillouin zone. Finally, note that in practice the field component $S_{(i)}^z(\mathbf{p})$ could be sufficient to distinguish between $\tilde{\nu}_i = 0$ and $\tilde{\nu}_i = \pm 1$ by counting the number of times $S_{(i)}^z$ takes extremal values over the Brillouin zone. An odd number of maxima, say three, over one minimum is obtained with the right configuration of Fig. 8, while even number of maxima and minima should correspond to winding number zero.

-
- [1] A. C. Potter and P. A. Lee, Phys. Rev. Lett. **105**, 227003 (2010).
 - [2] Y. Yu and Z. Wang, Europhys. Lett. **84**, 57002 (2008).
 - [3] V. Lahtinen *et al.*, Ann. Phys. **323**, 2286 (2008).
 - [4] W. S. Bakr *et al.*, Nature **462**, (2009).
 - [5] A. Klinger *et al.*, Rev. Sci. Instrum. **81**, 013109 (2010).